Supplementary Material: Channel Dynamics in an Experimental Alluvial Fan Under Constant Boundary Conditions: A Classification of Avulsion and Lateral Migration Events

Nastaran Nematollahi[1, 2], Brett Eaton[1, 2], and Sarah Davidson[1, 2]

[1]Department of Geography, University of British Columbia, 1984 West Mall, Vancouver, BC V6T 1Z2, Canada
[2]BGC Engineering Inc., 980 Howe Street, Vancouver, BC V6Z 0C8, Canada

Correspondence: Nastaran Nematollahi (nasipour@student.ubc.ca)

1 Supplementary Methods: Detailed Description

Here we provide additional details about the equipment, data sources, and preprocessing steps used in the experiment. Specifically, we describe the camera setup, the two datasets collected (3D photogrammetry images and high-frequency RGB images), and the methods applied to prepare these datasets for analysis.

S1.1 Equipment

A total of seven Canon EOS Rebel T6i DSLRs were used in the experiment. One camera was mounted directly overhead, 1.5 m above the center of the fan surface, oriented vertically downward, and captured RGB images at 3-second intervals to document surface flow patterns at high spatial and temporal resolution. The remaining six cameras were dedicated to Structure-from-Motion (SfM) photogrammetry for generating digital elevation models (DEMs). These cameras were mounted side-by-side on a rigid rail system positioned 1.0 m above the fan table. The rail was moved in 10 cm increments along the 2.5 m table length, and at each stop all six cameras were triggered simultaneously, producing 78 photographs per DEM acquisition. Based on the APS-C sensor size (22.3 × 14.9 mm), focal length of 18 mm, and camera height of 1.0 m, each image covered a ground footprint of ~1.2 × 0.8 m, yielding a ground sampling distance of ~0.24 mm/pixel and forward overlap of 88–92%. Photogrammetry image sets were collected every 30 minutes, after water flow had stopped and the fan surface had drained, ensuring a static, reflection-free bed. Camera positions are shown in the main manuscript (fig.1).

We conducted photogrammetry in Agisoft Photoscan Professional (Version 1.4.5, build 7354). The image sets were processed using high-quality settings for image alignment and aggressive filtering to generate dense topographic point clouds.Each dense cloud contained over 11 million points, yielding an average density of approximately 3.4 million points per square meter, equivalent to a mean point spacing of ~0.55 mm. From these point clouds, we produced DEMs at 0.5 $mm/pixel$ resolution.

All cameras were identical Canon EOS Rebel T6i DSLRs equipped with Canon EF-S 18–55 mm lenses fixed at 18 mm focal length. They were set to an aperture of f/10 and ISO 400, with focus adjusted manually before each experiment and autofocus disabled to maintain consistency. Illumination was provided by two LED lights positioned at the downstream corners, while
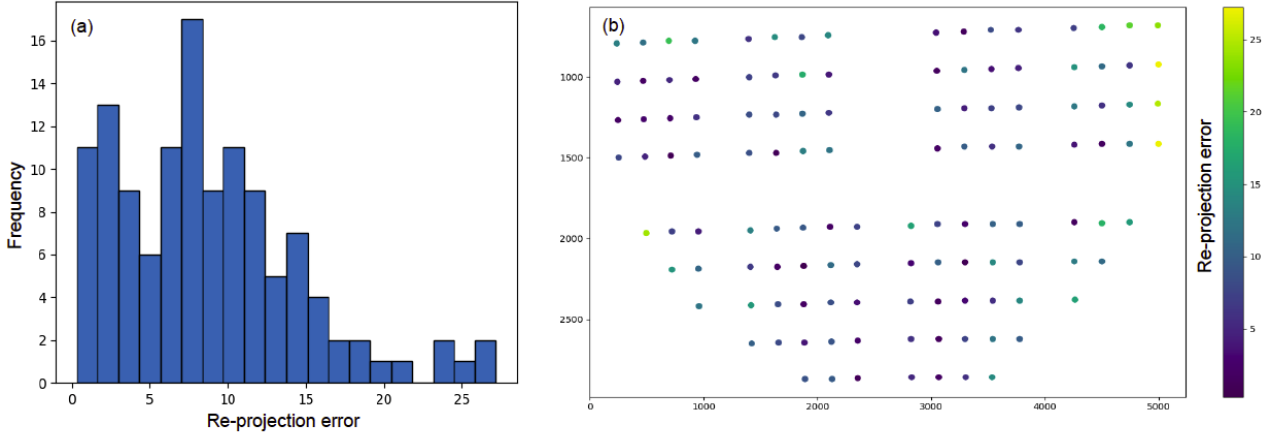
Figure S1. Distribution of re-projection errors following homography-based image transformation.

a translucent plastic sheet covered the setup to reduce glare from ceiling lights and daylight, ensuring uniform lighting and minimal shadowing across image sequences.

S1.2 Image preprocessing

Image preprocessing steps—including georectification, georeferencing, fan surface masking—and optical flow analyses were performed in Python using the OpenCV library (Bradski, 2000). All other analyses, including raster calculations and spatial analysis, were conducted in R using the Terra package (R Core Team, 2025; Hijmans, 2024). All scripts, along with a representative subset of the experimental dataset and animated videos of the experiment, are available in our GitHub repository.

S1.2.1 Image georectification and georeferencing

We corrected the radial distortion of the overhead Canon DSLR camera, which was installed for flow mapping, using Adobe Photoshop's Auto Lens Correction feature, which considers the camera-specific EXIF metadata to apply the appropriate distortion profile. Further, all the rectified images were georeferenced to our defined coordinate system using a reference orthophoto through a homography-based transformation. The accuracy of this alignment was calculated using the mean reprojection error—defined as the Euclidean distance between transformed points in the corrected image and their corresponding locations in the orthophoto—which was 10.11 pixels, equivalent to 10 mm. As shown in Figure 1 (b), the high values of reprojection errors are related to the left and right corners of the image beyond the maximum fan extent. An overlay of the transformed image on the reference orthophoto is presented in Figure 2.
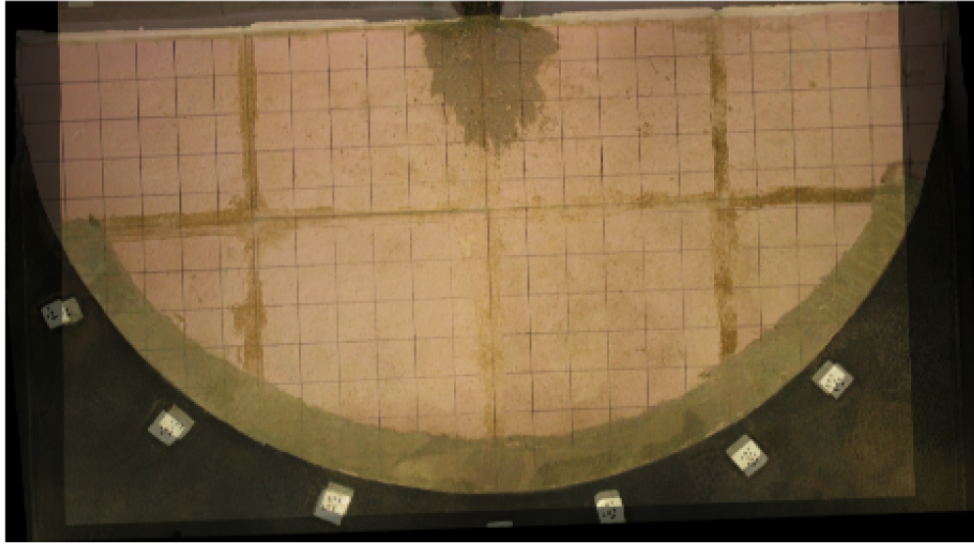
Figure S2. Overlay of orthophoto and transformed image post homography application.

S1.2.2   Fan surface masking

40   The overhead camera used to capture flow images had a wider field of view than the fan, including parts of the experimental setup and the sheet beneath the fan. To isolate the fan surface, we first applied a Gaussian blur with $\sigma = 5$ to reduce noise caused by grain texture and lighting variability. We then performed intensity thresholding using a value ranging from 112 to 117, which was empirically determined and visually inspected at regular intervals(every 600 images) to account for minor lighting changes over time. We further refined the resulting binary mask using a morphological erosion operation with a 3×3

45   kernel to eliminate small, isolated noise elements, as shown in Figure 3. The final binary mask was applied to each frame to isolate the active fan surface. These masked images were then used to calculate fan area and fan radius through time and to compile video sequences for optical flow analysis.

To assess how well the optical flow method identifies geomorphically active areas, we compared cumulative pixel-motion maps generated over 30-minute intervals with Difference of DEMs (DoDs), calculated between successive DEMs taken at the

50   beginning and end of each interval. As shown in Figure 3 (a) and (b), the sensitivity of the optical flow method—measured as the proportion of true geomorphic changes (identified by the DoD) that were correctly detected—remained consistently high, often exceeding 0.90. In contrast, the precision—measured as the proportion of optical flow detections that corresponded to true geomorphic changes approximately $51\% \pm 2.7\%$. Precision was highest during the early stages of the experiment and gradually declined in later phases, which can be attributed to the fan's lateral expansion into regions of the table with greater

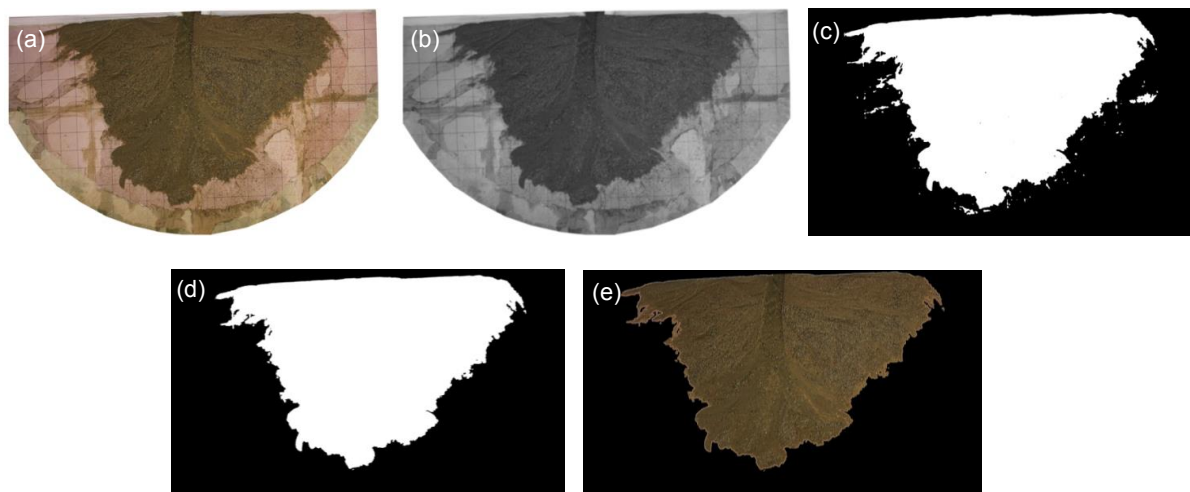55   photogrammetric distortion and reprojection error.

3

Figure S3. Preprocessing steps for isolating the fan surface. (a) Georeferenced and georectified image. (b) Smoothed image after applying a Gaussian blur filter. (c) Binary mask obtained through intensity-based thresholding. (d) Refined mask following a morphological erosion operation. (e) Final masked fan surface overlaid on the original image.

Some of the observed differences between the geomorphically active areas derived from optical flow and those derived from DoD are also related to ephemeral scour–fill cycles. These are short-lived processes in which water temporarily erodes a slight depression (scour) and deposits sediment into the same location (fill), resulting in negligible net elevation change. While the DoD captures only the net effect—often showing no change—the algorithm captures any pixel-level motion (change in intensity), including those that are reversed within minutes. Consequently, the cumulative flow maps may record surface activity that ultimately leaves no morphologic trace in the DEMs. From a geomorphological perspective, such ephemeral motion is important, as it reflects sediment transport dynamics, sorting, or channel reworking that precedes more permanent morphological adjustments. Thus, this discrepancy between optical flow and DoD is not necessarily a limitation but a complementary view: DoDs capture the outcome of change, while optical flow reveals the process. Together, they provide information about where and when the fan surface is in motion and whether that motion ultimately results in lasting morphodynamic change.

Although the 3-second frame interval allowed detection of broader zones of surface activity, it was insufficient to detect the displacement of individual grains. Moreover, because optical flow estimates apparent motion based on intensity changes rather than physical tracking of mass, the resulting flow fields do not represent true velocity fields. As noted by Liu and Shen (2008), the brightness constancy assumption foundational to optical flow is not derived from physical laws and may be violated by lighting changes, sediment disturbance, and water-surface reflections. Therefore, while optical flow provides a useful proxy for identifying zones of geomorphic activity, quantitative interpretation of displacement magnitudes would require independent calibration against known physical motion.
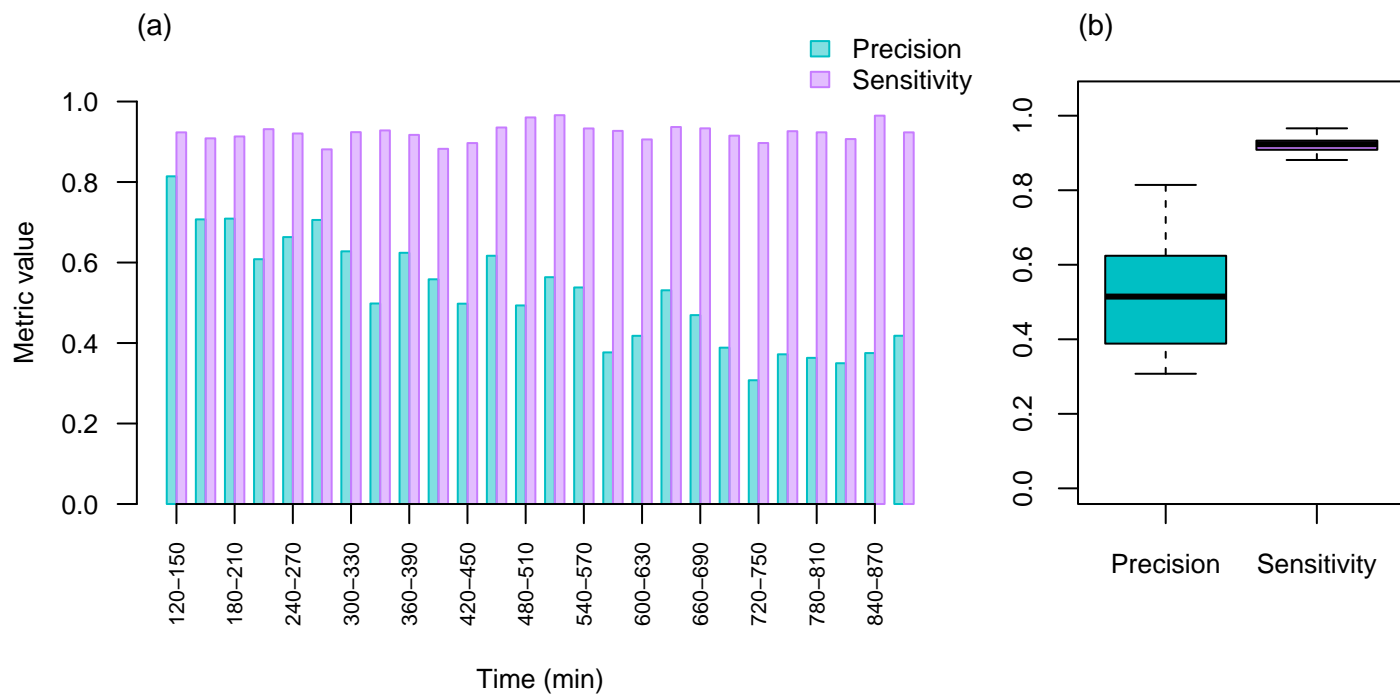
Figure S4. (a) Precision and sensitivity over time, compared to geomorphic change from DoDs. (b) Boxplots showing distributions across all intervals.
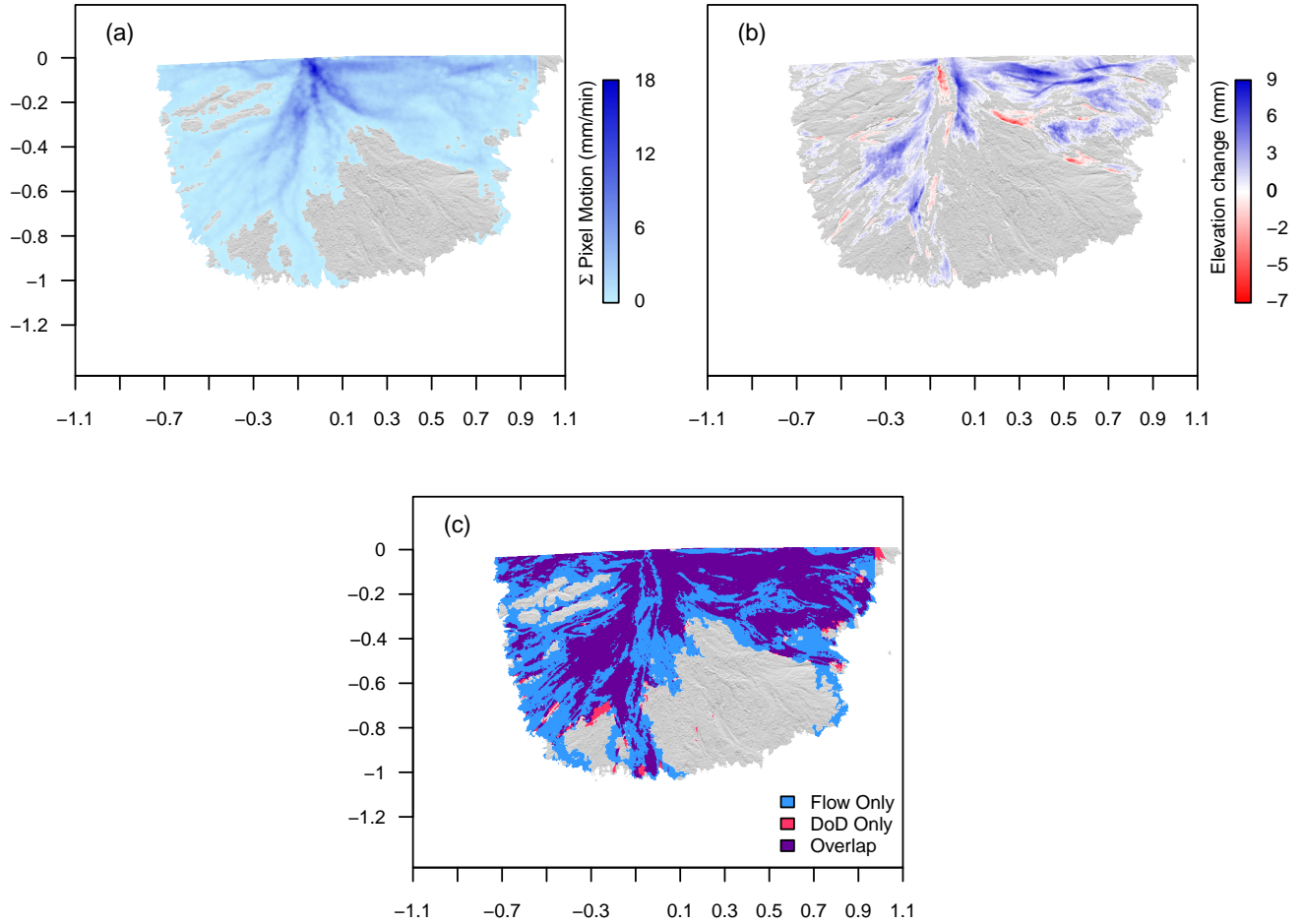
Figure S5. Comparison of active flow areas using (a) cumulative pixel motion from optical flow over 30 minutes of the experiment, indicating water and sediment movement, and (b) Difference of DEMs (DoD), showing sediment redistribution.

Code and data availability. The full source data for this study exceed 1 TB in size and are therefore not hosted online. Code and sample data are openly available at: https://github.com/Nastarannmt. The complete datasets are available from the corresponding author upon reasonable request.

Video supplement. The supplementary video presents a time-lapse sequence from 210 to 540 minutes of the 9-hour experiment. The initial 3.5 hours, during which the fan developed its baseline morphology, are excluded. The video therefore focuses on the period analyzed in the study, capturing the active phases of channel migration, reorganization, and avulsion.

Author contributions. NN designed and carried out the experiments, processed optical-flow maps and DEMs, analyzed results, and drafted the manuscript. BRE supervised the study, contributed to interpretation, and edited the manuscript. SD provided technical guidance and contributed to analysis and manuscript revisions.

Competing interests. The authors declare no competing interests.

Disclaimer. The authors used AI-assisted proofreading tools to improve grammar and clarity. All interpretations and conclusions are solely those of the authors.

References

Bradski, G.: The OpenCV Library, in: Dr. Dobb's Journal of Software Tools, 2000.

Hijmans, R. J.: terra: Spatial Data Analysis, https://cran.r-project.org/package=terra, r package version 1.7-78, 2024.

Liu, T. and Shen, L.: Fluid flow and optical flow, Journal of Fluid Mechanics, 614, 253–291, https://doi.org/10.1017/S0022112008003273, 2008.

R Core Team: R: A Language and Environment for Statistical Computing, R Foundation for Statistical Computing, Vienna, Austria, https://www.R-project.org/, 2025.

90